The shocking state of apatite and merrillite in shergottite Northwest Africa 5298 and extreme nanoscale chlorine isotope variability revealed by atom probe tomography

Journal Item

Journal Pre-proofs

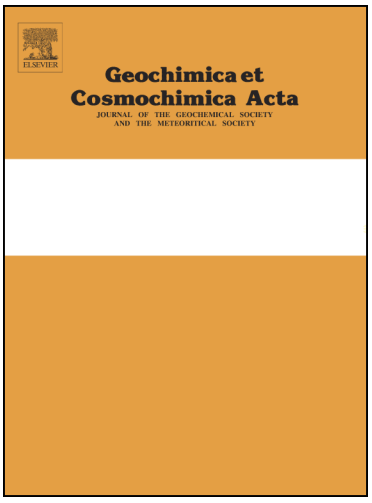

The shocking state of apatite and merrillite in shergottite Northwest Africa 5298 and extreme nanoscale chlorine isotope variability revealed by atom probe tomography

J.R. Darling, L.F. White, T. Kizovski, A. Černok, D.E. Moser, K.T. Tait, J. Dunlop, B. Langelier, J.O. Douglas, X. Zhao, I.A. Franchi, M. Anand

PII: S0016-7037(20)30682-7
DOI: https://doi.org/10.1016/j.gca.2020.11.007
Reference: GCA 11982

To appear in: *Geochimica et Cosmochimica Acta*

Received Date: 1 July 2020
Revised Date: 16 October 2020
Accepted Date: 9 November 2020

Please cite this article as: Darling, J.R., White, L.F., Kizovski, T., Černok, A., Moser, D.E., Tait, K.T., Dunlop, J., Langelier, B., Douglas, J.O., Zhao, X., Franchi, I.A., Anand, M., The shocking state of apatite and merrillite in shergottite Northwest Africa 5298 and extreme nanoscale chlorine isotope variability revealed by atom probe tomography, *Geochimica et Cosmochimica Acta* (2020), doi: https://doi.org/10.1016/j.gca.2020.11.007

The shocking state of apatite and merrillite in shergottite Northwest Africa 5298 and extreme nanoscale chlorine isotope variability revealed by atom probe tomography

Darling, J.R.[a*], White, L.F.[b,c], Kizovski, T.[b,c], Černok, A.[b,c], Moser, D.E.[e], Tait, K.T.[b,c], Dunlop, J.[a], Langelier, B.[f], Douglas, J.O.[g], Zhao, X.[d], Franchi, I.A.[d] & Anand, M.[d,h]

[a] School of the Environment, Geography and Geosciences, University of Portsmouth, Burnaby Building, Burnaby Road, Portsmouth, PO1 3QL, United Kingdom (*correspondence: james.darling@port.ac.uk)

[b] Centre for Applied Planetary Mineralogy, Department of Natural History, Royal Ontario Museum, 100 Queens Park, Toronto, Ontario, M5S 2C6, Canada

[c] Department of Earth Sciences, University of Toronto, Toronto, Ontario, M5S 3B1, Canada

[d] Planetary and Space Sciences, School of Physical Sciences, The Open University, Walton Hall, Milton Keynes, MK7 6AA, United Kingdom

[e] Zircon & Accessory Phase Laboratory (ZAPLab), Department of Earth Sciences, Western University, Biological & Geological Sciences Building, 1151 Richmond St. N., London, Ontario, N6A 5B7, Canada

[f] Canadian Centre for Electron Microscopy, McMaster University, A. N. Bourns Building B161, 1280 Main Street West, Hamilton, Ontario, L8S 4M1, Canada

[g] Department of Materials, University of Oxford, 16 Parks Road, Oxford, OX1 3PH, United Kingdom

[h] Department of Earth Sciences, The Natural History Museum, London, SW7 5BD, United Kingdom

Abstract

The elemental and chlorine isotope compositions of calcium-phosphate minerals are key recorders of the volatile inventory of Mars, as well as the planet's endogenous magmatic and hydrothermal history. Most martian meteorites have clear evidence for exogenous impact-generated deformation and metamorphism, yet the effects of these shock metamorphic processes on chlorine isotopic records contained within calcium phosphates have not been evaluated. Here we test the effects of a single shock metamorphic cycle on chlorine isotope systematics in apatite from the highly shocked, enriched shergottite Northwest Africa (NWA) 5298. Detailed nanostructural (EBSD, Raman and TEM) data reveals a wide range of distributed shock features. These are principally the result of intensive plastic deformation, recrystallization and/or impact melting. These shock features are directly linked with chemical heterogeneities, including crosscutting microscale chlorine-enriched features that are associated with shock melt and iron-rich veins. NanoSIMS chlorine isotope measurements of NWA 5298 apatite reveal a range of δ^{37}Cl values (-3 to 1 ‰; 2σ uncertainties <0.9 ‰) that is almost as large as all previous measurements of basaltic shergottites, and the measured δ^{37}Cl values can be readily linked with different nanostructural states of targeted apatite. High spatial resolution atom probe tomography (APT) data reveal that chlorine-enriched and defect-rich nanoscale boundaries have highly negative δ^{37}Cl values (mean of -15 ± 8 ‰). Our results show that shock metamorphism can have significant effects on chemical and chlorine isotopic records in calcium phosphates, principally as a result of chlorine mobilization during shock melting and

recrystallization. Despite this, low-strain apatite domains have been identified by EBSD, and yield a mean $\delta^{37}Cl$ value of -0.3 ± 0.6 ‰ that is taken as the best estimate of the primary chlorine isotopic composition of NWA 5298. The combined nanostructural, microscale-chemical and nanoscale APT isotopic approach gives the ability to better isolate and identify endogenous volatile-element records of magmatic and near-surface processes as well as exogenous, shock-related effects.

Highlights:

- Chlorapatites and merrillites in NWA 5298 have a wide-range of shock nanostructures
- Shock features in apatite are linked to elemental and chlorine isotope heterogeneity
- Atom probe tomography can yield accurate chlorine isotope data at ‰ precision
- Nanoscale boundaries contain isotopically light chlorine mobilized during shock
- The primary chlorine isotopic composition of NWA 5298 is -0.3 ± 0.6 ‰ (2σ)

1. Introduction

The calcium phosphate minerals apatite and merrillite have become very important to our understanding of planetary evolution and geological processes. They are now widely used to evaluate the origin, abundance and evolution of volatile species in planetary bodies (e.g. McCubbin et al., 2015; McCubbin and Jones, 2015; Barnes et al., 2016; Williams et al., 2016; Bellucci et al., 2017), provide thermochronological constraints on endogenic geological processes and meteorite impact events (Grange et al., 2013; Snape et al., 2016; Min et al., 2017), and track magmatic evolution through trace element and isotopic studies (Bruand et al., 2017). This is due to the incorporation of volatile species in apatite group minerals, hexagonal $Ca_5[PO_4]_3[F,Cl,OH]$, and the fact that both apatite and merrillite, trigonal $Ca_9Na(Fe,Mg)(PO_4)_7$, are the principal carriers of a wide-range of trace elements such as rare earth elements, uranium and thorium in many planetary crustal rocks.

In martian meteorites, the most abundant calcium phosphate phases are merrillite and chlorapatite. These phases are typically thought to crystallize in the late stages of magma evolution, and hence offer a unique window into the volatile inventory and magmatic processes within the martian interior (Filiberto and Treiman, 2009; McCubbin et al., 2012; Shearer et al., 2015). This has led to extensive efforts to characterize the water content, D/H ratio and chlorine isotopic composition of the martian mantle (e.g. Hallis et al., 2012; Sharp et al., 2016; Weis et al., 2017; Bellucci et al., 2017; Barnes et al., 2020).

Chlorine isotopes are particularly important, as they do not exhibit appreciable equilibrium isotopic fractionation at high temperatures (Sharp et al., 2016; Williams et al., 2016), and can therefore provide insights into the bulk composition of Mars and the materials from which it accreted, as well as the composition of the martian lithosphere and its interaction with the surface. Within the largest group of martian meteorites, basaltic to picritic igneous rocks known as shergottites, halogen contents and chlorine isotope ratios in apatite have been shown to be much more wide-ranging than in igneous rocks from Earth. There is up to ca. 6.6 ‰ variation in $\delta^{37}Cl$ ($^{37}Cl/^{35}Cl$ relative to standard mean ocean chloride, SMOC) between shergottites, which is hypothesized to reflect magmatic mixing between mantle and crustal reservoirs of chlorine (Sharp et al., 2016; Williams et al., 2016; Bellucci et al., 2017; Shearer et al., 2018; Roszjar et al., 2019). However, ambiguity remains in the chlorine isotopic composition of the martian mantle and in the causes of isotopic variability within groups of petrologically and chemically similar martian meteorites. An isotopically light martian mantle ($\delta^{37}Cl$ = -4 to -6 ‰) is supported by analyses of apatite in olivine-bearing shergottites and the dunite Chassigny (Sharp et al., 2016; Williams et al., 2016; Shearer et al., 2018). In contrast, in the samples measured by Bellucci et al., (2017), negative $\delta^{37}Cl$ values in phosphates were found to be associated with halogen enriched rims. These were interpreted to represent late-stage hydrothermal additions of chlorine, and these authors conclude that the martian mantle has a $\delta^{37}Cl$ identical to the terrestrial mantle ($\delta^{37}Cl$ of −0.6 ‰). Furthermore, there is up to ca. 5 ‰ variation among enriched basaltic shergottites. This is not well understood, given that these rocks are similar in texture, oxidation state,

trace elements and other isotope systems (e.g. Zagami, Shergotty and Los Angeles). Fully resolving chlorine isotope reservoirs on Mars is complicated by the possibility of surface reservoirs with both isotopically heavy and light chlorine (Farley et al., 2016; Bellucci et al., 2017). There is also evidence for volatile element heterogeneity within individual apatites that has been linked to secondary processes including impact melting and interaction with halogen-rich brines in martian near-surface environments (Howarth et al., 2015; Bellucci et al., 2017). The full range of causes of this variability and the influence on chlorine isotope systematics are not well understood.

Despite the highly-shocked nature of most martian meteorites, little is known about how many of the chemical and isotopic records in calcium phosphates respond to shock-metamorphism prior to or during launch in meteorite impacts. Martian meteorites have experienced shock pressures of at least ~5 GPa, constrained by the minimum impact energy required to eject material from the martian surface (Fritz et al., 2005), but most have petrological evidence for shock compression to many tens of GPa (Nyquist et al., 2001; Fritz et al., 2005). This evidence includes the conversion of plagioclase to diaplectic glass and/or impact melting. The potential importance of these processes to chemical records contained within calcium phosphates is highlighted by the recognition of shock-related devolatilization in apatite from NWA 7755 (Howarth et al., 2015; Wang et al., 2017) and the prospect that preserved (anhydrous) martian merrillite may have originally been hydrous whitlockite prior to shock events (Adcock et al., 2017). As such, shock metamorphic processes remain a significant unknown in assessing how representative the volatile contents of martian meteoritic apatite are of the planet's interior and near-surface reservoirs.

To test the structural and geochemical response of Ca-phosphates to shock metamorphism, here we present new chemical data for nanostructurally characterized chlorapatite and merrillite in the highly-shocked enriched basaltic shergottite NWA 5298, along with new chlorine isotope data from chlorapatite. We have combined nanostructural analysis by electron backscatter diffraction (EBSD), transmission electron microscopy (TEM) and Raman spectroscopy, chemical analysis by electron probe micro analysis (EPMA) and chlorine isotope ratio measurements of chlorapatite by nanoscale secondary ion mass spectrometry (NanoSIMS) and, for the first time, atom probe tomography (APT). Our results demonstrate that shock metamorphism has a major effect on the nanostructural state of Ca-phosphates, and that shock-induced structures lead to chemical and isotopic heterogeneities in apatite at the micro- to nano-scale. The new findings and methods have wide-ranging implications for studies of the volatile inventory and geo/thermochronology of planetary materials..

1.1. Known shock metamorphic microstructures in Ca-phosphates

A number of different microstructural features have previously been attributed to impact events in apatite and merrillite. These include planar features in apatite (Cavosie and Lugo Centeno, 2014; Słaby et al., 2017), fractured and brecciated apatite and merrillite in lunar breccias (Grange et al., 2013; Snape et al., 2016), partially melted apatite in martian meteorites (Greenwood et al., 2003;

Howarth et al., 2015), nanoscale mosaicism in martian apatite (Słaby et al., 2017), and formation of the high-pressure polymorph tuite from either phase transformation of whitlockite/merrillite or decomposition of apatite (Xie et al., 2002; Xie et al., 2013). A recent study of variably shocked Apollo 17 merrillite and fluorapatite shows that their microstructures become significantly more complex at higher levels of shock loading, notably reflected by increasing levels of crystal plastic deformation between shock stages S2 to S5, and recrystallization at S6 (Černok et al., 2019). Furthermore, Černok et al. (2020) show that shock nanostructures in these lunar samples facilitate migration of volatiles, resulting in a measureable effect on D/H in water poor apatite (<100 ppm H_2O). At extreme temperature conditions, recrystallization of apatite leads to phase separation and major element chemical heterogeneity (Kenny et al., 2019). However, understanding of whether these are representative of the full-range of shock microstructures in Ca-phosphates, and how they influence many volatile (e.g. F, Cl) or moderately volatile (e.g. Pb) species and isotopes, is currently lacking.

2. Sample and Methodology

2.1. Basaltic Shergottite Northwest Africa (NWA) 5298

The largest group of martian meteorites are ultramafic to basaltic igneous rocks known as shergottites, which represent ~75 separate falls and, with only two exceptions (NWA 4480 and NWA 12241; Irving et al., 2016; Lapen et al., 2019), are highly-shocked rocks (e.g. conversion of plagioclase to diaplectic glass). NWA 5298 is texturally and chemically similar to other basaltic shergottites, including Shergotty, Zagami and Los Angeles, but it has experienced higher degrees of shock deformation and metamorphism. The studied sample has a primary phaneritic igneous texture that is known to contain both chlorapatite and merrillite, which together make up ~2.1 % of the rock (Irving and Kuehner, 2008; Hui et al., 2011; Darling et al., 2016; Figure 1). In combination, this makes the sample ideally suited for investigation of the shock metamorphic response of elemental and isotopic systems in calcium phosphates.

Northwest Africa 5298 has experienced very high degrees of shock deformation and metamorphism. Shock features in the sample include vesicular plagioclase melt and diaplectic plagioclase-glass, highly fractured clinopyroxene, pockets of impact melt up to 3 mm in diameter, and partial granularization of clinopyroxene in contact with impact melt (Irving and Kuehner, 2008; Hui et al., 2011; Darling et al., 2016). Furthermore, it has been shown that the refractory accessory mineral baddeleyite (monoclinic-ZrO_2) in NWA 5298 has undergone variable U-Pb age resetting (i.e. grain-scale Pb-diffusion) due to shock-induced phase transformations and recrystallization resulting from decompression at high temperatures (Moser et al., 2013; Darling et al., 2016). Shock transformation of plagioclase (An_{40-55}; Hui et al., 2011) to diaplectic glass and vesicular melt suggests a shock pressure of at least 29 GPa (Stöffler et al. 1986), and NWA 5298 shares many characteristics of shock stage mafic (M)-S5 of (Stöffler et al., 2018), which these authors conclude to require equilibrium

shock pressure of >42 GPa. Irrespective of the absolute bulk shock pressure experienced by NWA 5298, these petrological features place the meteorite towards the higher end of the range of shock metamorphic conditions experienced by shergottites. Importantly, the shock pressures experienced by individual accessory minerals in the sample have been shown to be highly variable, due to differences in the shock impedance of surrounding major phases (Darling et al., 2016). Analyses were performed on a single polished thin-section of the sample; accession number M53387 from the Royal Ontario Museum's collection.

2.2. Electron Imaging, X-ray microanalysis and Electron Backscattered Diffraction (EBSD)

Scanning electron microscopy (SEM) was undertaken at the University of Portsmouth, utilizing a Zeiss EVO MA10 SEM fitted with a LaB_6 electron source. Prior to imaging, the sample was vibratory polished (Buehler VibroMet 2) for 10 minutes using a 0.05 μm alumina suspension (pH = 7) to remove surface defects, and then carbon coated. Calcium-phosphates were located from energy-dispersive X-Ray spectroscopy (EDS) maps, collected using an Oxford Instruments X-Max 80 detector. Subsequently, apatite and merrillite were identified by semi-quantitative spot analyses and imaged by secondary electron (SE) and backscattered electron (BSE) detectors using an accelerating voltage of 15 kV and probe currents of between 0.2 and 1 nA. Further EDS maps were collected of selected apatite and merrillite targets using these conditions.

Lattice orientation, internal microtexture, and structural (dis)order of selected apatites and merrillites were studied by EBSD. After SEM imaging, the carbon coat was removed using isopropanol and 0.05 μm alumina, and then EBSD analyses undertaken using Oxford Instruments Nordlys-nano EBSD detector mounted on the same SEM at the University of Portsmouth, UK. Data were processed using Oxford Instruments Aztec software, and then further analysis of EBSD data was undertaken using the Channel 5 software suite. Diffracted electrons were collected at a tilt angle of 70°, using a primary electron beam with 20 kV accelerating voltage and 1 nA probe current in variable-pressure mode (N_2 was used to maintain chamber pressure of 20-30 Pa), broadly following the approach of Darling et al., (2016), White et al., (2017) and Papapavlou et al., (2018). Diffraction patterns were automatically captured and indexed every 50 to 500 nm across manually defined areas. Apatite diffraction patterns were indexed to the chlorapatite crystal lattice parameters of (Hughes et al., 1989). Merrillite was indexed against the trigonal crystal parameters of (Xie et al., 2015). Tuite, the high pressure calcium phosphate polymorph, was included for indexing in all analyses using the structural details of (Thompson et al., 2013), but no coherent domains were indexed with confidence (e.g. mean angular deviation <1). Wild spike reduction was conducted on all datasets, though no other form of raw data correction was undertaken. Instrumental parameters and operating conditions are detailed in Supplementary Table 1.

2.3. Electron Probe Microanalysis (EPMA)

The major element and volatile compositions of selected merrillite and apatite targets were determined using the JEOL JXA-8230 electron microprobe at Queen's University, Canada. Hydroxyl compositions in apatite can be inferred when fluorine and chlorine concentrations are known (OH, F and Cl occupy the anion site in apatite which is assumed to add up to 1 atom per formula unit; McCubbin & Jones, 2015). In order to use this technique, great care must be taken to effectively analyse fluorine and chlorine, as they are highly mobile under an electron beam. Accordingly, instrument conditions were optimized for low beam currents, based on those outlined by Goldoff et al. (2012), and with the use of a LDE1 diffracting pseudocrystal in order to accurately measure fluorine (McCubbin et al., 2016; McCubbin et al., 2018). Beam conditions of 10 kV accelerating voltage and 4 nA beam current were first used to measure fluorine, chlorine and sodium, followed by analysis of the remaining elements at 15 kV and a 20 nA beam current, all with a defocussed 5–10 μm spot size.

Instrument conditions were checked against well-known secondary standard Durango fluorapatite in both basal and prismatic orientations (Supplementary Table 2). Even with the low beam current, fluorine X-ray count rates were observed to change based on crystallographic orientation (as previously observed by Stormer et al., 1993). Fluorine concentrations measured in the Durango standard oriented with its c-axis parallel to the beam are consistently higher than those measured with its c-axis perpendicular to the beam (average F concentrations of 3.79 wt.% and 3.54 wt.%, respectively). Fluorine concentrations measured in basal orientation consistently exceed 3.76 wt.%, the maximum possible in stoichiometric fluorapatite (Pyle et al., 2002; Goldoff et al., 2012). No other elements appeared to be significantly affected by orientation changes. Additional challenges to EPMA measurements of NWA 5298 apatite are presented by inclusion trails and veins, principally of iron-rich material, and the wide range of acceptable totals is due to the possibility of up to 1.79 wt.% H_2O (inferred from OH^- content) in apatite, and up to 8500 ppm H_2O in whitlockite that cannot be detected by EPMA. Accordingly, if analytical totals were outside of the range 97.0–102.0 wt.% for apatite or 97.5–101.5 wt.% for merrillite, the analysis was discarded (McCubbin et al., 2015; Shearer et al., 2015). The results are presented in Supplementary Tables 3 and 4 and analysis positions shown in Supplementary Figure 1. Detection limits were calculated at the 3σ level.

2.4. Micro-Raman Spectroscopy

Raman spectra were collected for apatite and merrillite using a Horiba LabRAM ARAMIS Raman Spectrometer, housed at the Royal Ontario Museum. A 532 nm laser was used with the laser power filtered down to approximately 2.1 mW to prevent sample damage. A 1200 groove/mm grating and 150 μm slit were used during collection. Depending on the objective selected (x50 or x10), resulting spot sizes ranged from 0.9 to 2.6 μm. Spectrum collection times varied between 8 and 120 seconds per point. High resolution maps were created by analysing points at 1.5-5 μm increments across Ca-phosphates (areas ranging from 0.008 to 0.16 mm^2); with the goal of identifying any high pressure

phases (tuite), and to identify peak shifts and changes in peak widths in the Raman spectra across the areas of interest. These differences can correspond to variable mineral compositions, and/or possibly different levels structural disorder and shock (i.e. Černok et al., 2019). LabSpec 6 software was used to apply polynomial baseline corrections to the collected spectra. The curve fitting and data analysis program Fityk 0.9.8 (Wojdyr, 2010) was used to measure the position and full width half maxima (FWHM) of the peaks; assuming Lorenztian peak shapes. Representative Raman spectra from Ca-phosphates in NWA 5298 is shown in Supplementary Figure 2

2.5. NanoSIMS chlorine isotope measurements

The CAMECA NanoSIMS 50L secondary ion mass spectrometer at the Open University was used to measure the chlorine abundance and isotopic composition of selected apatites in NWA 5298. The chosen analytical positions were more than 10 microns away from those of prior EPMA or Raman spot analyses. Before each analysis, a Cs^+ ion beam with a current of 100 pA was rastered over 7x7 μm^2 sample areas for 3 minutes to remove the gold coating and possible surface contamination. Subsequently, a 25 pA Cs^+ ion beam was used to carry out measurements from the inner 5 x 5 μm^2 areas. The negative secondary ions of $^{16}O^1H$, ^{18}O, ^{19}F, ^{35}Cl, ^{37}Cl and $^{40}Ca^{16}O$ were collected simultaneously using electron multipliers. Real-time ion imaging of OH, Cl and CaO were also monitored before and after each analysis for locating apatite and avoiding cracks. The mass resolving power was set to ~8000 (CAMECA definition), enough to resolve isobaric interferences such as ^{17}O from $^{16}O^1H$. Chlorine abundances were calibrated using measured $^{35}Cl/^{18}O$ and three terrestrial apatite reference materials; Ap004, Ap005 and Ap018 from McCubbin et al., (2012). Background estimation of chlorine (~1 ppm) was carried out using San Carlos olivine. Apatite standard Ap005 was used to correct the measured chlorine isotopic compositions for instrumental mass fractionation. Detailed descriptions of the protocols and calculations can be found in Barnes et al., (2016). The calculated $^{37}Cl/^{35}Cl$ ratios are reported relative to standard mean ocean chloride (SMOC): $\delta^{37}Cl$ (‰) = $([^{37}Cl/^{35}Cl]_{measured} / [^{37}Cl/^{35}Cl]_{SMOC} - 1) * 1000$.

2.6. Transmission Electron Microscopy (TEM) and Atom Probe Tomography (APT)

Samples for TEM and APT analysis were prepared using an FEI Scios 3D Focussed Ion Beam (FIB) equipped with field emission electron and Ga^+ ion sources at the Warwick Manufacturing Group, University of Warwick. Prior to FIB milling, a ~1 µm Pt layer was deposited over target areas to protect the surface from ion-beam induced damage. For preparation of the TEM foil, initial milling of the trenches and shaping of the liftout used a 30 kV, 15 nA Ga^+ ion beam. The liftout was then extracted and mounted using a platinum weld, and subsequently thinned and polished using 3 nA to 0.3 nA ion beam. A final polish using a rastered 5 kV, 48 pA Ga^+ ion beam was undertaken to remove surface damage from previous steps. For preparation of APT needles, similar ion-beam parameters were applied using standard lift-out and mount techniques to produce the desired specimen shape

(Thompson et al., 2007). A series of annular mills were used to produce needle-shaped specimens with a radius of curvature less than ~100 nm. A final, low energy polish (5 kV, 48 pA) was applied to remove defects and ion implantation induced by the milling procedure.

TEM analyses were undertaken using an FEI Talos F200X field emission TEM, equipped with 4 Bruker EDS detectors, at the Warwick Manufacturing Group, University of Warwick. TEM images were collected at 200 kV with a bright field (BF) detector, and STEM images collected using both BF and high angular annular dark field (HAADF) detectors. EDS spectrum maps were collected using Bruker software.

APT analyses were conducted in two analytical sessions, using a local electron atom probe (LEAP) 4000X HR at the Canadian Centre for Electron Microscopy (CCEM), McMaster University, Canada, and LEAP 5000X HR at the University of Oxford, UK. Prepared microtip specimens were held in the instrument under vacuum (~4 x 10^{-11} torr) in cryogenic conditions (~50-60 K base temperature), and a pulsed laser was used to induce ionic evaporation at the tip of the specimen and simultaneous measurement of masses from 0-300 Da using time-of-flight mass spectrometry and a position-sensitive micro-channel plate detector. Full instrumental conditions are reported in Supplementary Table 5, and are based on those reported by (Gordon et al., 2012). Reconstruction of APT data was conducted using Integrated Visualization and Analysis Software (IVAS 3.6.14), using established methods (Gault et al., 2012) and by integrating the measured voltage curve. Ranging of the spectra was conducted manually, constraining elemental and isotopic peaks that are then background corrected and quantified by the IVAS software package. The range file was altered to facilitate subtle peak shifts within each dataset, typically no more than ~0.1 Da on the largest peaks. Background counts were calculated for each ranged peak by extrapolating the surrounding spectrum counts linearly within the defined range. Cluster-finding analysis was performed by using the nearest neighbour distance frequency distribution of atoms and cluster analysis tool in IVAS 3.6.14, following the approaches described in Dhara et al., (2018). For Mn and Fe, these approaches identified clusters comparable to those shown by isoconcentration surfaces.

Due to the very high detection efficiency of APT instruments (36-52 % in the instruments used in this study), it has been shown that accurate isotopic ratio measurements are possible without a correction for instrumental mass bias or external normalization, even for inter-elemental ratios such as $^{206}Pb/^{238}U$ (White et al., 2017; White et al., 2018). Accordingly, chlorine isotope ratios were calculated from the background-corrected peaks at 35 and 37 Da without additional standardization or correction. These peaks fall within a section of the mass spectrum with a smooth background and few other species (Supplementary Figure 3). A fixed-width of mass-window was applied to all Cl peaks (± 0.08 Da). A sample of Madagascar pegmatite fluorapatite (MAD; 0.22 ± 0.1 wt. % Cl; Chew et al., 2014) was analysed to refine measurement conditions. The accuracy of chlorine isotope ratio measurements using APT was monitored using MAD and by comparison of APT and NanoSIMS measurements from the same NWA 5298 apatite. The MAD fluorapatite is assumed to have a

chlorine isotope composition ($\delta^{37}Cl$) of between -4 to +3 ‰, which is the total range of igneous and metamorphic rocks on Earth (Barnes and Sharp, 2017; majority have $\delta^{37}Cl$ of 0 ± 0.5 ‰). Uncertainties were calculated by propagating the counting statistics uncertainty on the background corrected peak, with the precision of the local background for each peak. The latter was modelled from the exported mass spectrum using a linear regression, with a fixed background range of ± 0.5 Da from the peak centre mass.

3. Results

Apatites occur in interstitial sites between clinopyroxene, (former) plagioclase and Fe-Ti-oxide crystals (**Figure 1**). Merrillite is more abundant and occurs with a broader range of textural settings, including interstitial sites alongside apatite, within clinopyroxene and intergrown with (former) plagioclase. Both phases can be found within impact melt pockets, but there is no clear association between impact melt and calcium-phosphate abundance. Furthermore, there is no apparent link between fractures or veins and calcium-phosphate occurrence or texture. These observations are supportive of an igneous origin for both phases, consistent with interpretations from studies of other martian meteorites (Filiberto and Treiman, 2009; McCubbin et al., 2012; Shearer et al., 2015; Bellucci et al., 2017). Detailed SEM imaging was undertaken on six apatite and ten merrillites, from which four of each were selected for EBSD analysis. In SE and BSE images, the majority appear smooth and relatively featureless apart from crosscutting fractures and veins of variable composition. However, EBSD analysis has revealed a range of micro- to nano-scale structural features in both phases.

3.1. Apatite micro- to nano-structures

Despite most apatites appearing smooth and relatively featureless in BSE imaging, all of the apatites studied by EBSD have a complex nanoscale structure with highly variable degrees of lattice disorder. This is well expressed by band contrast (BC), a quality factor that describes the average intensity of the Kikuchi bands with respect to the overall intensity within the electron backscatter pattern (EBSP). As shown in **Figure 2**, BC maps reveal micro- to nano-scale domains of strongly diffracting apatite surrounded by networks of weakly diffracting material, including sub-micron spaced sets of planar-features. The variable orientation of these features between and within apatites, along with the high-quality of surface polishing revealed by forescattered electron imaging, demonstrates that these are inherent structural characteristics. This is further supported by maps of crystallographic orientation (e.g. inverse pole figure, IPF; **Figure 2A,B**; **Figure 3A,B**), which reveal that many of these weakly diffracting domains have a high density of low-angle boundaries (2-10°; hereafter termed subgrain boundaries). Together with typical misorientations of 1-5° across the more strongly diffracting domains, these features accommodate many tens of degrees of total misorientation (**Figure 2A,B**). As such, the majority of apatites in NWA 5298 record evidence for intensive plastic

deformation. Some of the studied apatites are also cross-cut by veins of glassy material that we interpret to be impact melt. Qualitative EDS analysis reveals these to be comprised predominantly of Si and Al, or Fe (e.g. **Figure 2A**).

Micro-Raman spectroscopy corroborates that apatite is the chlorine-bearing calcium-phosphate phase, with all collected spectra having a principal intense peak at 962-963 cm^{-1} that is consistent with previous data from chlorapatite (e.g. Xie et al., 2013; Supplementary Figure 2). Raman maps show that the intensity of this principal peak varies at the microscale, with areas of weakly diffracting or nanocrystalline material in EBSD analysis also having less intense and broader Raman peaks. Lower intensities of this peak are also observed in regions where apatites are crosscut by impact melt veins. Raman mapping did not unambiguously identify any areas of tuite, which has characteristic peaks at 977 cm^{-1} or 1096 cm^{-1} (Xie et al., 2013; Litasov and Podgornykh, 2017) .

A single apatite within an impact melt pocket shows significantly different structural characteristics (Apatite 2; **Figure 2C**). This apatite shows variability in BSE contrast, and strings of Fe-oxides are interpreted as evidence of flow-texture after partial melting and injection of Fe. It has a highly complex structure with nanoscale domains predominantly separated by high-angle boundaries (>10°; hereafter termed grain boundaries) and scattered orientations on pole-figures that are representative of recrystallization. Domains with brighter BSE and without Fe-rich inclusions have lower band contrast and record one principal (if highly-deformed and partially recrystallized) orientation. This is interpreted as partial preservation of the original unmelted grain, which is further supported by the fact that these domains yield more intense 962-963 cm^{-1} peaks in Raman analysis than surrounding nanocrystalline domains with Fe-rich inclusions.

Apatite 3 (**Figure 2B**) was selected for further detailed analysis, as it represents an excellent example of an apatite with preserved areas of low internal misorientation, surrounded by poorly-diffracting regions with a high-density of subgrain boundaries and some grain boundaries. Furthermore, SEM-EDS X-ray mapping shows significant heterogeneity in Cl and Fe contents. Notably, this includes broad concentric zoning in Cl, cross-cutting Cl-enriched features, and Fe-rich cross-cutting veins that are low in Cl (**Figure 3A**; Supplementary Figure 4). There is no clear correlation of Cl or Fe concentration with the degree of local misorientation (**Figure 3B**), however the cross-cutting Cl-enriched features correspond to occurrences of grain boundaries (**Figure 3C**). Scanning-TEM (STEM) and TEM analysis of a liftout across these features further emphasizes the complex nanocrystalline state of the material, with a subgrain structure comprised of variably strained 5-400 nm domains, including some with planar-features, separated by defect-rich boundaries (**Figure 3D,E,F**). Many of the larger nanodomains have straight or gently-curved boundaries and form a polygonal structure that provides evidence for partial recrystallization. STEM-EDS analysis reveals that many of these boundaries have resolvable enrichments in Fe, that chlorine concentration varies between nanoscale domains, and that there are subtle variations in Ca at the nanoscale (**Figure 3E**).

3.2. Merrillite micro- to nano-structures

Similarly to apatite, the BSE images of merrillite in NWA 5298 show little contrast, but do highlight cross-cutting fractures and occasional brighter Fe-rich cross-cutting veins (**Figure 4**). The EBSD data again reveals a complex internal structure within the merrillites, with areas of strongly diffracting material surrounded by networks of subgrain boundaries that have lower BC values (**Figure 4A,B**). The merrillites are highly strained, with tens of degrees of total misorientation occurring across most of the studied targets. One significant difference from the apatite data is the occurrence of micron to sub-micron scale domains with high-angle boundaries to the host and apparently random crystallographic orientations. These neoblasts occur along networks of subgrain boundaries and are interpreted to reflect partial recrystallization. Similar features have been reported from other accessory phases, including monazite ([La,Ce,Th]PO_4; (Erickson et al., 2017)), zircon (Moser et al., 2011) and titanite (Papapavlou et al., 2018). Some regions (e.g. Merrillite 4; Figure 4A) show an even more complex structure dominated by poorly diffracting nanoscale domains that could not be readily indexed given the interaction volume of our EBSD analyses (tens of nanometres depth). As such, it is likely that parts of the merrillite are variably ordered at length scales of less than ~50 nm, or amorphous.

3.3. Electron probe microanalysis (EPMA) results

A total of 26 EPMA analyses of apatite were undertaken, and the results are presented in Supplementary Tables 3 and 4. The apatites without evidence for shock melting have a range of measured Cl (1.57-3.03 wt. %), F (0.66-1.67 wt. %) and calculated H_2O contents. They also have variable quantities of SiO_2 (0.50-1.17 wt %), FeO (1.02-1.89 wt. %), SO_3 (0.13-0.45 wt. %) and MnO (0.01-0.17 wt. %), along with minor Al_2O_3, TiO_2, Na_2O and K_2O that are above detection limits in some analyses. These variations are as large within individual grains as they are between grains. A ternary plot of X-site occupancy highlights the variability in apatite composition in NWA 5298 (**Figure 5**), and the overall intermediate composition in terms of Cl, F and OH contents that is similar to other enriched shergottites such as Shergotty (McCubbin et al., 2012). Data from the three analysed grains shows signficant intra- and inter-grain spread of Cl, F and OH contents; with no unambiguous link between volatile content and density of subgrain boundaries (**Figure 5**). This implies that the calculated volatile contents are either relatively insensitive to subgrain boundary formation, or that any possible influence on volatile contents is restricted to recrystallization and/or structures at the sub-micron scale (i.e. smaller than EPMA interaction volumes).

Impact melting has a clear influence on the chemistry of apatites in NWA 5298. The melted and recrystallized regions have resolvably higher (with 2σ uncertainties) FeO (2.38-3.38 wt. %), Al_2O_3 (0.01-0.15 wt. %) and TiO_2 (0.11-0.15 wt.%). The Cl and F contents are highly variable, but within the range of unmelted grains.

Target	Analysis ID	Nanostructure	Cl (ppm)	2σ	$\delta^{37}Cl_{SMOC}$ (‰)	2σ
Ap1	Ap1b	High density SGB	25880	540	-3.15	0.81
	Ap1a	High density SGB	21620	530	-2.96	0.86
Ap2	Ap2b	Annealed primary apatite	14610	520	-1.09	0.88
	Ap2a	Melted region	21850	510	1.08	0.75
Ap3	Ap3b	Low density SGB	15510	520	-0.26	0.83
	Ap3a	Low density SGB	23970	560	-0.41	0.82

Table 1: NanoSIMS chlorine isotope compositions and chlorine contents from apatites in NWA 5298, compared to identified nanostructural state of the measured region (SGB = subgrain boundaries).

A total of 24 EPMA measurements were made of merrillites from two distinct textural settings. Merrillites 3, 4 and 5 occur within a mass of Fe-Ti-oxides, whereas two targets labelled merrillite 2 occur in an interstitial site between clinopyroxene and diaplectic plagioclase-composition glass, in association with vesicular plagioclase melt. The latter group have higher FeO and MnO, and lower MgO and Na_2O contents. It has previously been shown that merrillite in martian meteorites has a wide range of Mg# ($[Mg_{atomic}/(Mg_{atomic}+Fe_{atomic})]*100$), which is correlated with Na and Mn contents as a reflection of the pre-merrillite crystallization history of the melts (Shearer et al., 2015). The Mg# of merrillite intergrown with Fe-Ti-oxides (Merrillite 3; Mg# 19.5 to 23.0) is significantly higher than a merrillite located within an interstitial site between pyroxene and (former) plagioclase (Merrillite 2; Mg# 11.8 to 15.2), which is consistent with merrillite crystallization from an evolving melt composition, or from late interstitial melt of varying composition.

3.4. NanoSIMS chlorine isotope results

A total of six NanoSIMS measurements were made of three apatites in NWA 5298, targeting the different nanostructural states identified by EBSD and Raman spectroscopy (Table 1). These yielded Cl contents consistent with those measured by EPMA, and a range of $\delta^{37}Cl$ that is as large as the range of all previous measurements from basaltic shergottites. There is a clear relationship between nanostructures and measured $\delta^{37}Cl$. The single positive measured ratio (1.08 ± 0.75 ‰) comes from a region of apatite 2 with evidence for melting and recrystallization. The most negative values (-3 ‰) were measured in domains of apatite 1 with a high-density of subgrain boundaries (see **Figure 2** for analysis locations). Intermediate $\delta^{37}Cl$ values (-0.26 ± 0.83 ‰, -0.41 ± 0.82 ‰) were measured from the least nanostructurally complex apatite, Apatite 3, in areas with lower densities of subgrain boundaries, as well as from an annealed primary apatite domain in apatite 2 (-1.09 ± 0.88 ‰).

3.5. Atom probe tomography (APT) results

APT analyses were performed on a tip from the MAD Madagascar pegmatite fluorapatite (Chew et al., 2014), and five tips from a single liftout from Apatite 3. These tips were extracted across the Cl enriched >10° grain boundary identified by SEM-EDS and EBSD analysis, from regions with both high and low density of subgrain boundaries (See **Figure 3A** for liftout location). A total of 39

million ions were collected from the MAD tip, and from 5 to 41 million in each of the NWA 5298 tips. As previously shown for apatite (Gordon et al., 2012), the APT mass spectra are complex and dominated by calcium, oxygen and various phosphorous oxide, chloride and fluoride peaks. Nevertheless, a number of additional elements and isotopes were confidently identified, including F, Na, Mg, Si, Cl, Mn, Fe, Sr, Y, Ce and Pb (Supplementary Figure 3 and Supplementary Table 6).

In MAD, all ions and compounds appear homogeneously distributed (Supplementary Figure 5). Major elements (Ca, P, O) in the NWA 5298 datasets have only small variations in concentration, but there are some striking heterogeneities in the concentration of some minor and trace elements. These are most clearly observed in the distribution of Fe atoms (**Figure 6**), with 4 to 6 atom percent (at. % Fe) isoconcentration surfaces defining planar, curved and clustered regions that are equivalent in scale to Fe-enriched grain and subgrain boundaries observed via STEM (**Figure 3E**). Proximity histograms to these isoconcentration surfaces reveal that Fe contents in these structures reach as high as 10 %, with a corresponding decrease in O, Ca and P content compared to the host apatite. The Cl content within these nanoscale boundaries is variable, but on average slightly enriched compared to bulk tips (Table 1). Cl and Fe are decoupled in these boundaries, with Fe defining wave-like structures similar to features observed in shocked baddeleyite (White et al., 2017). Relative to the bulk-tips, the Fe-rich features are also resolvably enriched in Si and Pb (supplementary Table 6). In addition to Fe, clustering of Mn is also defined by 1-2 at. % isoconcentration surfaces (**Figure 6**), although these clusters are more broadly distributed throughout the datasets.

Several different chlorine species were identified from the APT mass spectra (Supplementary Figure 3). From highest to lowest confidence in identification (and also abundance), these were Cl^+, ClO^+, $CaCl^+$ and PO_2Cl^+. The calculated background-corrected Cl concentration of the MAD fluorapatite tip is 0.19 ± 0.01 wt. %, (all uncertainties 2σ) which is similar to the published value of 0.22 ± 0.01 wt. % from microscale LA-ICP-MS analysis (Chew et al., 2014). The NWA 5298 APT tips also yield Cl concentrations (1.18 to 2.52 wt. %) within the range measured by EPMA and NanoSIMS (1.46 to 2.59 wt. %), providing confidence that the major Cl species have been identified. The calculated $\delta^{37}Cl$ value for MAD fluorapatite is 2.9 ± 13 ‰ , within uncertainty of the composition of all igneous rocks from Earth (~0 ‰), albeit with large uncertainties due to limitations in counting statistics. Chlorine isotope results for the NWA 5298 APT tips are presented in Table 2. The values from individual tips range from -12.5 ± 4.8 ‰ to 3.7 ± 5.3 ‰, and the concatenated dataset (all APT tips linked into one mass spectra) has a $\delta^{37}Cl$ value of -1.7 ± 2.2 ‰, which is within uncertainty of the NanoSIMS results from the same apatite (-0.26 ± 0.83 and -0.41 ± 0.82 ‰; **Figure 7B**). There is no discernible correlation between Cl concentration and $\delta^{37}Cl$ amongst the APT data. The isolated Fe-rich features and planar boundaries have highly-negative $\delta^{37}Cl$ (-12.0 ± 4.2 to -45.3 ± 17.8 ‰), albeit with large uncertainties due to the limitations of counting statistic uncertainties (**Figure 7B**).

		Fe (at. %)	Cl (at. %)	^{35}Cl (cts)	2σ (cts)	^{37}Cl (cts)	2σ (cts)	$\delta^{37}Cl_{SMOC}$ (‰)	2σ (‰)
MAD Fluorapatite Bulk Tip									
R83_02915		0.04	0.19	13747	266	4405	159	2.9	13.1
NWA 5298 Bulk Tips									
R47_01717	Tip 5	0.81	2.24	79127	618	25397	372	3.7	5.3
R47_01719	Tip 2	0.76	2.22	85935	616	27137	360	-12.5	4.8
R47_01721	Tip 6	0.46	2.99	127495	754	40628	442	-3.5	3.9
R83_02916	Tip 4	0.62	1.57	61598	528	19546	306	-7.7	5.7
R83_02919	Tip 3	0.63	1.18	18328	326.8	5898	208	6.4	12.7
NWA 5298 Nanoscale boundaries									
R47_01717	Boundary (Fig. 6)	1.25	2.28	8156	212	2490	130	-45.3	17.8
R47_01719	4 % Fe ICS	5.64	2.53	7339	206	2253	124	-40.0	19.0
R47_01721	3 % Fe ICS	3.70	3.31	113367	713	35817	419	-12.0	4.2
R83_02916	2.5 % Fe ICS	3.91	1.80	3304	147	1024	94	-30.6	31.6
Concatenated NWA 5298 dataset									
Overall				381344	1279	121732	742	-1.7	2.2

Table 2: Chlorine isotopic compositions and background corrected chlorine contents measured by atom probe tomography in NWA 5298 Apatite 3 and MAD fluorapatite. Note that the concatenated NWA 5298 dataset result is within uncertainty of NanoSIMS results from this apatite.

4. Discussion

4.1. Shock effects on martian apatite and merrillite

Phosphate minerals have been intensively deformed during the single shock event that has affected NWA 5298 (Darling et al., 2016). Both chlorapatites and merrillites record tens of degrees of total misorientation and high-densities of subgrain boundaries. These structural features are broadly similar to those recently identified in fluorapatite and merrillite in lunar rocks of approximately equivalent bulk shock stage (S5; (Černok et al., 2019), but our findings add important new detail to the understanding of shock effects in calcium-phosphates. Notably, it is clear that shock structures are highly variable within and between Ca-phosphates in a single thin section. This is consistent with understanding that the peak shock pressure and waste heat experienced on the micrometer-scale can vary by a factor of two or more, due to differing shock impedance of surrounding phases (Sharp and de Carli, 2006; Darling et al., 2016). We have identified different apatite domains with evidence for planar deformation features, melting and recrystallization, annealing, high-densities of subgrain boundaries and low-densities of subgrain boundaries within the studied thin-section. The latter domains are interpreted to represent preserved primary apatite that has not undergone major structural modification (e.g. **Figure 3**C). Of the range of analytical techniques used in this study, only EBSD is able to readily identify these low-strain apatite domains at the microscale. It is important to note that highly shock-deformed and/or recrystallized apatite domains in this study still yield intense Raman peaks, and more work is needed to determine whether peak intensity and

broadening can be used as a predictive tool for shock deformation in calcium-phosphates. Merrillite in NWA 5298 has similar levels of overall misorientation to apatite, but shows a greater tendency to form neoblasts with high-angle grain boundaries in response to post-shock heating.

Chemical heterogeneities occur within NWA 5298 apatites at a range of scales, and these can be linked to the evolution of shock-induced structures. While the formation of planar features during shock loading is not commonly associated with diffusion and chemical exchange in accessory minerals (e.g. Moser et al., 2011), the apatites have also undergone intensive plastic deformation. This is thought to be associated with relatively late stage shock-decompression at high temperatures and high-strain rates (Moser et al., 2011; Timms et al., 2012). Plastic deformation of apatite results in complex nanostructural states defined by high-densities of dislocations (Saka et al., 2008). Recovery of these defects could explain the abundance of subgrain boundaries observed in NWA 5298 apatite. The occurrence of some polygonally structured domains also provides evidence for partial recrystallization, and post-shock heating driven by impact melt has also caused partial recrystallization of titanomagnetite and clinopyroxene in the sample (Darling et al., 2016). Atom probe tomography and STEM-EDS analysis demonstrate that Fe and some trace elements (Si and Pb), are enriched in these nanoscale boundaries. Additional evidence for mobility of minor and trace elements is provided by nanoclustering of Fe and Mn atoms throughout the APT datasets.

Atom probe tomography and STEM data provide evidence for both short-range mobilization of these elements and the potential for open system behaviour along boundaries. NWA 5298 is lacking evidence for intensive hydrothermal alteration at the microscale (Hui et al., 2011), but there is clear evidence in the sample for the mobilization of Fe as a result of shock melting of sulphides and Fe-Ti oxides. This can be seen as cross-cutting Fe-rich veins that extend from recrystallized iron-titanium-oxide grains, as well as strings of Fe-rich inclusions in the shock-melted apatite domains. It is possible that external Fe has been mobilized into apatite along nanoscale grain boundaries, which are known to remain open systems for trace element mobility in other mineral phases (Fougerouse et al., 2019). Despite this, only the shock-melted apatite domains have bulk Fe-contents that are unusually high (i.e. >2 wt. % FeO) for apatite from basaltic shergottites. The unmelted NWA 5298 apatite domains have similar FeO content (mean = 1.43 wt. %) to apatite in some other less-shocked basaltic shergottites, including Los Angeles, Shergotty, QUE 94201, NWA 2975 and NWA 2986 and NWA 8656 (Barrat et al., 2002; McCubbin et al., 2012; McCubbin et al., 2016; Slaby et al., 2016). There is no clear link between FeO content measured by EPMA and the density of either high-angle or low-angle nanoscale boundaries in different unmelted grain domains, which argues against Fe-enrichment on these features being principally controlled by infiltration of Fe from surrounding phases. Furthermore, nanoclustering of trace elements similar to those seen for Fe and Mn in NWA 5298 apatite has been documented in a wide-range of accessory mineral phases, including zircon, baddeleyite and the rare earth element phosphate, monazite, where it has been linked with short-range diffusion during high-temperature metamorphism (e.g. Valley et al., 2014; White et al., 2017;

Seydoux-Guillaume et al., 2019). Taken together, this provides evidence for significant internal mobilization of Fe and trace elements into defect-rich boundaries and clusters.

Evidence for mobilization of chlorine in NWA 5298 apatite is principally provided by micron-width high-Cl bands that cross-cut apatites along grain boundaries (e.g. **Figure 3**A; Supplementary Figure 4). These have not been observed away from chlorapatite in the thin section and are associated with similar scale veins of alumino-silicate shock melt. Accordingly, it is likely that these represent Cl-rich fluids exsolved from apatite associated with melting. Similar Cl-enriched features have previously been linked to devolatilization of apatite in contact with shock melt, and/or the partial transformation to tuite (Howarth et al., 2015; Wang et al., 2017). The fact that these Cl-rich veins are observed to crosscut sharp concentric zoning in Cl-content within Apatite 3 suggests that this process is facilitated by shock microstructures. Chlorine enrichment is also observed in nanoscale boundaries and domains in STEM and APT data, indicating that chlorine has been mobilized along structures at a range of scales. At the microscale volume of EPMA measurements, F/Cl ratios are highly variable, at a similar extent to apatite in the less intensively shocked shergottites such as Shergotty (Patiño Douce and Roden, 2006; McCubbin et al., 2012).

4.2. Microscale chlorine isotope heterogeneity in NWA 5298 apatite

Variations in chlorine isotope ratios between martian meteorites are well documented. The basaltic shergottites range in apatite δ^{37}Cl values from -3.8 to +1.0 ‰ (Sharp et al., 2016; Williams et al., 2016; Bellucci et al., 2017; Roszjar et al., 2019). This is thought to reflect variable magmatic mixing between mantle (-4 to -6 ‰) and crustal (>0 ‰) reservoirs of chlorine (Williams et al., 2016; Shearer et al., 2018), but this record is complicated by evidence for secondary modification of chlorine in martian meteorite apatite. Notably Bellucci et al., (2017) document apatites within enriched olivine-phyric shergottite Larkman Nunatuks (LAR) 12011 that have grain margins enriched in halogens and negative δ^{37}Cl values (-4.0 to -5.6 ‰), which they ascribe to interaction with halogen-rich brines in the martian near-surface.

Our new linked nanostructural and NanoSIMS results from NWA 5298 show that microscale chlorine isotopic variability in apatite can be as large within a single basaltic shergottite as the total range in measured values from this sample suite (**Figure 7**). The fact that the measured δ^{37}Cl values can be readily linked with different nanostructural states suggests that shock-metamorphism of NWA 5298 apatite has facilitated heterogeneity in chlorine isotope ratios. The measured domain with evidence for impact melting has the highest δ^{37}Cl value (1.08 ± 0.75 ‰), which is consistent with preferential loss of isotopically light chlorine or impact melt interaction with an isotopically heavy surface reservoir (Williams et al., 2016; Shearer et al., 2018). In contrast to Bellucci et al., (2017) the most negative δ^{37}Cl values in our dataset (ca. -3 ‰) are not associated with halogen-enriched rims, but rather chlorine-rich grain domains with high-densities of subgrain boundaries (HD-SGB) that have up to 10 wt. % Fe (Supplementary Table 6). If the chlorine and iron within HD-

SGB domains originated externally to the apatites, then it would be expected to carry the same isotopic signature as melted iron-rich grain domains. Instead, this data suggests that internal micro- to nano-scale redistribution of chlorine, iron and trace elements was dominant, and that shock-generated defects may preferentially facilitate mobilization of isotopically light chlorine.

Our best estimate of the primary chlorine isotope composition of NWA 5298 is provided by NanoSIMS measurements of nanostructurally simple apatite domains (low densities of SGB), which yield an average δ^{37}Cl value of -0.3 ± 0.6 ‰ (n = 2). This value is within uncertainty of apatite and bulk-rock chlorine isotope measurements of other enriched basaltic shergottites that are petrologically and geochemically similar to NWA 5298, notably NWA 2975, Los Angeles and Zagami (Williams et al., 2016; Bellucci et al., 2017).

4.3. Nanoscale chlorine isotope heterogeneity in NWA 5298 apatite revealed by APT

Further insights into chlorine isotope heterogeneity are provided by APT, which we use for the first time to investigate chlorine isotopes at the nanoscale. The fact that the concatenated δ^{37}Cl value from APT analysis of NWA 5298 apatite (-1.7 ± 2.2 ‰) is within uncertainty of NanoSIMS measurements from the same grain, as well as the results from the MAD reference fluorapatite, demonstrates that accurate chlorine isotope measurements are possible from chlorapatite using APT. This approach has revealed extreme nanoscale chlorine isotope heterogeneity in Apatite 3, despite overall agreement between measurements at the larger volumes of the concatenated dataset (total analytical volume ~0.005 μm^3) and NanoSIMS (~25 μm^3). The 5-10 nm wide Fe and Cl enriched domains within unmelted apatite revealed by TEM and APT have highly negative measured δ^{37}Cl values, with a weighted mean of -15 ± 8 ‰ (2σ; n = 4). This demonstrates that nanoscale boundaries are facilitating the movement of isotopically light chlorine. The exact origin of this chlorine is not easily identified, however there are a number of lines of evidence that suggest internal remobilization from within apatite, rather than externally derived fluids: (1) Cl-enriched domains are not associated with elevated concentrations of other halogens that are expected in near-surface brines (Bellucci et al., 2017); (2) there are no mineralogical or chemical signatures in the sample of other known martian fluids, which produce smectite-group clay minerals, Ca-sulphates, Mg-sulphates and the K-Fe–sulphate jarosite as alteration assemblages (Mustard, 2019); (3) these shock-generated nanoscale boundaries have a distinct isotopic composition from Fe-rich partially melted microscale grain domains; (4) the nanoclustering of trace elements, such as observed in NWA 5298 apatite, is a distinct feature of very high temperature metamorphism (i.e. granulite facies or shock metamorphism). As such, we interpret that mobilization of isotopically-light chlorine has occurred as a result of shock melting and recrystallization of apatite, in a process akin to observed chlorine enrichment surrounding shock melt in NWA 7755 (Howarth et al., 2015).

5. Conclusions

Nanostructural analysis of apatite and merrillite in the highly shocked basaltic shergottite NWA 5298 has revealed a wide-range of impact generated nanostructures in both phases. These are the result of shock-loading, extensive crystal plastic deformation, recrystallization and/or partial melting, which have variably affected different Ca-phosphates in the studied thin-section.

Chemical and chlorine isotope measurements of these different domains has revealed new links between shock metamorphism and chemical exchange in apatite. At the microscale, there is evidence for the exsolution of chlorine-rich fluids from apatite in contact with impact melt. At the nanoscale, transmission electron microscopy and atom probe tomography show that some minor and trace elements have been mobilized into defect-rich nanoscale boundaries (Fe, Si and Pb) and others into clusters (Fe and Mn).

NanoSIMS chlorine isotope measurements of NWA 5298 apatite reveal a range of δ^{37}Cl values (-3 to 1 ‰) that is almost as large as all previous measurements of basaltic shergottites. The measured δ^{37}Cl values can be readily linked with different nanostructural states of targeted apatite, indicating that shock-metamorphism has directly influenced chlorine isotope ratios.

Atom probe tomography has been used to determine chlorine contents and isotope ratios for the first time, and we demonstrate that accurate chlorine isotope ratios can be measured by this approach. This is most clearly demonstrated by consistency between NanoSIMS and APT results from the same NWA 5298 chlorapatite. Application to NWA 5298 apatite has revealed that nanoscale grain domains, including defect-rich nanoscale boundaries, have highly negative δ^{37}Cl values (-15 ± 8 ‰), which we interpret to have resulted from mobilization of isotopically light chlorine during the shock event.

Despite the complex shock-history of these apatites, low-strain domains have been identified and targeted for chlorine isotope measurements. The primary δ^{37}Cl composition of NWA 5298 is -0.3 ± 0.6 ‰. Our findings underline the need to carefully characterize the nanostructural state of Ca-phosphates in meteorites in order to fully understand volatile element and isotopic records of planetary evolution. The new combined NanoSIMS and atom probe tomography approach has tremendous potential to resolve primary and secondary isotopic compositions of challenging planetary samples.

6. Acknowledgements

This work was supported by Royal Society grant RG160237 and STFC grants ST/S000291/1 and ST/T002239/1 to JRD and ST/P000657/1 to MA and IAF, along with UoP support for FIB-SEM and TEM access. AČ and LFW acknowledge the Hatch Ltd. Fellowship. TVK acknowledges the Hatch University Graduate Fund and the support of the Natural Sciences and Engineering Research Council of Canada (NSERC; funding reference #CGSD2 - 534938 – 2019). We are grateful to the Executive Editor Jeff Catalano and to Associate Editor Chris Herd for their expert editorial handling,

and to two anonymous reviewers for their detailed and constructive reviews that helped to improve the paper. We are also grateful to Geoff Long for sample preparation wizardry at UoP and Geoff West for assistance with FIB-SEM and TEM analysis at Warwick. The LEAP 5000XR at the Department of Materials, Oxford was funded by EPSRC (EP/M022803/1).

7. Figure Captions

Figure 1: Backscattered electron (BSE) image showing the distribution of chlorapatite (green) and merrillite (blue) in NWA 5298. Chlorapatites occur in interstitial sites, whereas merrillite occurs in a broader range of textural settings. There is no clear association between impact melt and calcium-phosphate abundance.

Figure 2: Chlorapatite nanostructures in NWA 5298. (A) typical of most studied apatites, Apatite 1 is relatively featureless in BSE, beyond some fracturing, however in EBSD band contrast (BC) and inverse pole figure maps (IPF-Z) a complex nanostructure is defined by a high-density of subgrain boundaries (HD-SGB; grey lines on IPF-Z map) that accommodate tens of degrees of total misorientation; (b) similar to apatite 1, but has micron-scale domains with low-densities of subgrain boundaries (LD-SGB) and was selected for further TEM and APT analysis (Figure 3); (C) apatite within an impact melt pocket that has variable BSE contrast and strings of Fe-rich material that are interpreted as evidence of melting. Nanoscale domains are separated by both subgrain and grain boundaries (>10°, red lines on IPF-Z). The positions of NanoSIMS Cl-isotope analyses are shown by 5x5 μm squares in BC images, along with measured $\delta^{37}Cl_{SMOC}$.

Figure 3: Nanostructure and chemical variations in Apatite 3. (A) Cl X-ray map highlighting sharp zoning and cross cutting Cl-rich and Cl-poor features, and also showing the location of TEM and APT lift-outs; (B) calculated local misorientation in degrees from a 3x3 pixel sampling of EBSD data, showing variably strained domains; (C) IPF-Z map with grain boundaries (red, >10°) and subgrain boundaries (grey, 2-10°); (D & E) example STEM data showing complex nanocrystalline state and enrichment of Fe along nanoscale boundaries in the area shown by box in D. Subtle variations are also observed in Cl, but these are difficult to discern from background noise using this technique; (F) bright field TEM data highlighting subgrain structure including variably strained 5-400 nm domains, including some with planar-features, separated by defect-rich boundaries that in some cases intersect at 120° triple-junctions.

Figure 4: Nanostructures in merrillites from NWA 5298. (A) Similarly to apatite, the BSE images are smooth textured and highlight fracturing and occasional Fe-rich cross-cutting veins (~1 μm in width and brighter in BSE). EBSD data reveals networks of subgrain boundaries (grey lines) accommodating tens of degrees of total misorientation, as shown by rotation on the pole figures. Nanoscale neoblasts with high-angle subgrain boundaries to the host are shown by major changes in IPF colouring and scattered orientations on pole figures. (B) Two merrillites grouped together as

Merrillite 2 showing further examples of cross-cutting Fe-rich veins and a highly strained structure, with neoblasts formed in regions with a high density of subgrain boundaries. EBSD map locations are shown by white rectangles in BSE images.

Figure 5: Ternary plot of apatite X-site occupancy from NWA 5298 apatites (Ap.1-3). Symbols differentiate analyses from domains with a low density of subgrain boundaries (LD-SGB; 2-10°), from those with a high density of subgrain boundaries (HD-SGB) and grain boundaries (GB; >10°), as well as recrystallized apatite following impact-melting (melted).

Figure 6: Atom probe tomography datasets from NWA 5298 chlorapatite. Selected isoconcentration surfaces (ICS) are shown for each whole dataset (Fe = blue, Cl = green, Mn = red) and examples of Fe and Cl enriched boundaries (lower right; viewed perpendicular to boundary surface).

Figure 7: (A) new NanoSIMS data from NWA 5298 chlorapatite, compared to previous measurements of apatite in olivine-phyric and basaltic shergottites (Williams et al., 2016; Bellucci et al., 2017; Roszjar et al., 2019) and the estimated martian mantle composition of (Shearer et al., 2018). (B) chlorine isotope data derived from atom probe tomography mass spectra, comparing the bulk composition of individual tips with isolated Fe-rich features and the concatenated dataset (all APT datasets linked into one mass spectrum). All uncertainties are reported at 2σ level.

8. References

Adcock C. T., Tschauner O., Hausrath E. M., Udry A., Luo S. N., Cai Y., Ren M., Lanzirotti A., Newville M., Kunz M. and Lin C. (2017) Shock-transformation of whitlockite to merrillite and the implications for meteoritic phosphate. *Nat. Commun.* **8**, 14667. Available at: http://www.nature.com/doifinder/10.1038/ncomms14667.

Barnes J. D. and Sharp Z. D. (2017) Chlorine isotope geochemistry. *Non-Traditional Stable Isot.* **82**, 345–378.

Barnes J. J., McCubbin F. M., Santos A. R., Day J. M. D., Boyce J. W., Schwenzer S. P., Ott U., Franchi I. A., Messenger S., Anand M. and Agee C. B. (2020) Multiple early-formed water reservoirs in the interior of Mars. *Nat. Geosci.* **13**, 260–264. Available at: http://dx.doi.org/10.1038/s41561-020-0552-y.

Barnes J. J., Tartèse R., Anand M., McCubbin F. M., Neal C. R. and Franchi I. A. (2016) Early degassing of lunar urKREEP by crust-breaching impact(s). *Earth Planet. Sci. Lett.* **447**, 84–94. Available at: http://dx.doi.org/10.1016/j.epsl.2016.04.036.

Barrat J. A., Gillet P., Sautter V., Jambon A., Javoy M., Göpel C., Lesourd M., Keller F. and Petit E. (2002) Petrology and chemistry of the basaltic shergottite North West Africa 480. *Meteorit. Planet. Sci.* **37**, 487–499. Available at: https://linkinghub.elsevier.com/retrieve/pii/S0016703702009341.

Bellucci J. J., Whitehouse M. J., John T., Nemchin A. A., Snape J. F., Bland P. A. and Benedix G. K. (2017) Halogen and Cl isotopic systematics in Martian phosphates: Implications for the Cl cycle and surface halogen reservoirs on Mars. *Earth Planet. Sci. Lett.* **458**, 192–202. Available at: http://linkinghub.elsevier.com/retrieve/pii/S0012821X16305854 [Accessed November 11, 2016].

Bruand E., Fowler M., Storey C. and Darling J. (2017) Apatite trace element and isotope applications to petrogenesis and provenance. *Am. Mineral.* **102**, 75–84.

Cavosie A. J. and Lugo Centeno C. (2014) Shocked Apatite from the Santa Fe Impact Structure (USA): A New Accessory Mineral for Studies of Shock Metamorphism. In *Lunar and Planetary Science Conference* Lunar and Planetary Science Conference. p. 1691.

Cernok A., Anand M., Zhao X., Darling J. R., White L. F., Stephant A., Dunlop J., Tait K. T. and Franchi I. A. (2020) Preservation of primordial signatures of water in highly-shocked ancient lunar rocks. **544**.

Černok A., White L. F., Darling J., Dunlop J. and Anand M. (2019) Shock-induced microtextures in lunar apatite and merrillite. *Meteorit. Planet. Sci.* **54**, 1262–1282. Available at: https://onlinelibrary.wiley.com/doi/abs/10.1111/maps.13278.

Chew D. M., Donelick R. A., Donelick M. B., Kamber B. S. and Stock M. J. (2014) Apatite Chlorine Concentration Measurements by LA-ICP-MS. *Geostand. Geoanalytical Res.* **38**, 23–35.

Darling J. R., Moser D. E., Barker I. R., Tait K. T., Chamberlain K. R., Schmitt A. K. and Hyde B. C. (2016) Variable microstructural response of baddeleyite to shock metamorphism in young basaltic shergottite NWA 5298 and improved U–Pb dating of Solar System events. *Earth Planet. Sci. Lett.* **444**, 1–12. Available at: http://linkinghub.elsevier.com/retrieve/pii/S0012821X16301194.

Dhara S., Marceau R. K. W., Wood K., Dorin T., Timokhina I. B. and Hodgson P. D. (2018) Atom probe tomography data analysis procedure for precipitate and cluster identification in a Ti-Mo steel. *Data Br.* **18**, 968–982. Available at: http://dx.doi.org/10.1016/j.dib.2018.03.094.

Erickson T. M., Timms N. E., Kirkland C. L., Tohver E., Cavosie A. J., Pearce M. A. and Reddy S. M. (2017) Shocked monazite chronometry : integrating microstructural and in situ isotopic age data for determining precise impact ages. *Contrib. to Mineral. Petrol.* **172**, 1–19.

Farley K. A., Martin P., Jr P. D. A., Atreya S. K., Conrad P. G., Eigenbrode J. L., Fairén A. G., Franz H. B., Freissinet C., Glavin D. P., Mahaffy P. R., Malespin C., Ming D. W., Navarro-gonzalez R. and Sutter B. (2016) Light and variable 37 Cl / 35 Cl ratios in rocks from Gale Crater , Mars : Possible signature of perchlorate. *Earth Planet. Sci. Lett.* **438**, 14–24. Available at: http://dx.doi.org/10.1016/j.epsl.2015.12.013.

Filiberto J. and Treiman A. H. (2009) Martian magmas contained abundant chlorine, but little water. *Geology* **37**, 1087–1090. Available at: https://pubs.geoscienceworld.org/geology/article/37/12/1087-1090/103856.

Fougerouse D., Reddy S. M., Kirkland C. L., Saxey D. W., Rickard W. D. and Hough R. M. (2019) Time-resolved, defect-hosted, trace element mobility in deformed Witwatersrand pyrite. *Geosci. Front.* **10**, 55–63. Available at: https://doi.org/10.1016/j.gsf.2018.03.010.

Fritz J., Artemieva N. and Greshake A. (2005) Ejection of Martian meteorites. *Meteorit. Planet. Sci.* **40**, 1393–1411.

Gault B., Moody M. P., Cairney J. M. and Ringer S. P. (2012) *Atom probe microscopy*., Springer Science & Business Media.

Goldoff B., Webster J. D. and Harlov D. E. (2012) Characterization of fluor-chlorapatites by electron probe microanalysis with a focus on time-dependent intensity variation of halogens. *Am. Mineral.* **97**, 1103–1115.

Gordon L. M., Tran L. and Joester D. (2012) Atom probe tomography of apatites and bone-type mineralized tissues. *ACS Nano* **6**, 10667–10675.

Grange M. L., Nemchin A. A. and Pidgeon R. T. (2013) The effect of 1.9 and 1.4 Ga impact events on

4.3 Ga zircon and phosphate from an Apollo 15 melt breccia. **118**, 2180–2197.

Greenwood J. P., Blake R. E. and Coath C. D. (2003) Ion microprobe measurements of18O/16O ratios of phosphate minerals in the Martian meteorites ALH84001 and Los Angeles. *Geochim. Cosmochim. Acta* **67**, 2289–2298.

Hallis L. J., Taylor G. J., Nagashima K. and Huss G. R. (2012) Magmatic water in the martian meteorite Nakhla. *Earth Planet. Sci. Lett.* **359–360**, 84–92. Available at: http://dx.doi.org/10.1016/j.epsl.2012.09.049.

Howarth G. H., Pernet-Fisher J. F., Bodnar R. J. and Taylor L. A. (2015) Evidence for the exsolution of Cl-rich fluids in martian magmas: Apatite petrogenesis in the enriched lherzolitic shergottite Northwest Africa 7755. *Geochim. Cosmochim. Acta* **166**, 234–248.

Hughes J. M., Cameron M. and Crowley K. D. (1989) Structural variations in natural F, OH, and Cl apatites. *Am. Mineral.* **74**, 870–876.

Hui H., Peslier A. H., Lapen T. J., Shafer J. T., Brandon A. D. and Irving A. J. (2011) Petrogenesis of basaltic shergottite Northwest Africa 5298: Closed-system crystallization of an oxidized mafic melt. *Meteorit. Planet. Sci.* **46**, 1313–1328. Available at: http://onlinelibrary.wiley.com/doi/10.1111/j.1945-5100.2011.01231.x/full.

Irving A. J., Andreasen R., Righter M., Lapen T. J., Busemann H., Izawa M., Moser D. E. and Sipiera P. P. (2016) Northwest Africa 4480 Revisited: Petrologic, Isotopic, and Noble Gas Studies of an Unshocked, Maskelynite-Free Mafic Shergottite with a Long Cosmic Ray Exposure Age. In *Lunar and Planetary Science Conference* Lunar and Planetary Science Conference. p. 2330.

Irving A. J. and Kuehner S. M. (2008) Northwest Africa 5298: A Strongly Shocked Basaltic Shergottite Equilibrated at QFM and High Temperature. *Meteorit. Planet. Sci. Suppl.* **43**, 5332.

Kenny G. G., Karlsson A., Schmieder M., Whitehouse M. J., Nemchin A. A. and Bellucci J. J. (2019) Recrystallization and chemical changes in apatite in response to hypervelocity impact. *Geology*.

Lapen T. J., Righter M., Irving A. J., Kuehner S. M., Carpenter P. K., Gessler N., Aid M., Aaronson A., M. A. and Hoefnagels B. (2019) Martian meteorite rain: petrology, elemental and isotopic composition of ten recently recovered shergottites. *50th Lunar Planet. Sci. Conf.* **Abstract #**, 49–50.

McCubbin F. M., Boyce J. W., Srinivasan P., Santos A. R., Elardo S. M., Filiberto J., Steele A. and Shearer C. K. (2016) Heterogeneous distribution of H 2 O in the Martian interior: Implications for the abundance of H 2 O in depleted and enriched mantle sources. *Meteorit. Planet. Sci.* **51**, 2036–2060.

McCubbin F. M., Hauri E. H., Elardo S. M., Vander Kaaden K. E., Wang J. and Shearer C. K. (2012) Hydrous melting of the martian mantle produced both depleted and enriched shergottites.

Geology **40**, 683–686.

McCubbin F. M. and Jones R. H. (2015) Extraterrestrial apatite: Planetary geochemistry to astrobiology. *Elements*.

McCubbin F. M., Vander Kaaden K. E., Tartèse R., Klima R. L., Liu Y., Mortimer J., Barnes J. J., Shearer C. K., Treiman A. H., Lawrence D. J., Elardo S. M., Hurley D. M., Boyce J. W. and Anand M. (2015) Magmatic volatiles (H, C, N, F, S, Cl) in the lunar mantle, crust, and regolith: Abundances, distribution, processes, and reservoirs. *Am. Mineral.* **100**, 1668–1707.

McCubbin F. M., Phillips B. L., Adcock C. T., Tait K. T., Steele A., Vaughn J. S., Fries M. D., Atudorei V., Kaaden K. E. V. and Hausrath E. M. (2018) Discreditation of bobdownsite and the establishment of criteria for the identification of minerals with essential monofluorophosphate (PO3F2-). *Am. Mineral.* **103**, 1319–1328.

Min K., Farah A. E., Lee S. R. and Lee J. I. (2017) (U-Th)/He ages of phosphates from Zagami and ALHA77005 Martian meteorites: Implications to shock temperatures. *Geochim. Cosmochim. Acta* **196**, 160–178. Available at: http://dx.doi.org/10.1016/j.gca.2016.09.009.

Moser D. E., Cupelli C. L., Barker I. R., Flowers R. M., Bowman J. R., Wooden J. and Hart J. R. (2011) New zircon shock phenomena and their use for dating and reconstruction of large impact structures revealed by electron nanobeam (EBSD, CL, EDS) and isotopic U-Pb and (U-Th)/He analysis of the Vredefort dome. *Can. J. Earth Sci.* **48**, 117–139.

Moser D. E. E., Chamberlain K. R. R., Tait K. T. T., Schmitt A. K. K., Darling J. R. R., Barker I. R. R. and Hyde B. C. C. (2013) Solving the Martian meteorite age conundrum using micro-baddeleyite and launch-generated zircon. *Nature* **499**, 454–457. Available at: http://www.nature.com/nature/journal/v499/n7459/abs/nature12341.html.

Mustard J. F. (2019) Sequestration of Volatiles in the Martian Crust Through Hydrated Minerals: A Significant Planetary Reservoir of Water. *Volatiles in the Martian Crust*, 247–263. Available at: https://www.sciencedirect.com/science/article/pii/B9780128041918000088 [Accessed March 9, 2020].

Nyquist L. E., Bogard D. D., Greshake A. and Eugster O. (2001) Ages and geologic histories of Martian meteorites. *Chronol. Evol. Mars*, 105–164.

Papapavlou K., Darling J. R., Moser D. E., Barker I. R., EIMF, White L. F., Lightfoot P. C., Storey C. D. and Dunlop J. (2018) U--Pb isotopic dating of titanite microstructures: potential implications for the chronology and identification of large impact structures. *Contrib. to Mineral. Petrol.* **173**, 82. Available at: https://doi.org/10.1007/s00410-018-1511-0.

Patiño Douce A. E. and Roden M. (2006) Apatite as a probe of halogen and water fugacities in the terrestrial planets. *Geochim. Cosmochim. Acta* **70**, 3173–3196. Available at: http://www.sciencedirect.com/science/article/pii/S0016703706001608.

Roszjar J., Whitehouse M. J., Terada K., Fukuda K., John T., Bischoff A., Morishita Y. and Hiyagon H. (2019) Chemical, microstructural and chronological record of phosphates in the Ksar Ghilane 002 enriched shergottite. *Geochim. Cosmochim. Acta* **245**, 385–405. Available at: https://doi.org/10.1016/j.gca.2018.11.015.

Saka H., Goto D. and Moon W. J. (2008) Dislocations in plastically deformed apatite. *J. Mater. Sci.* **43**, 3234–3239.

Seydoux-Guillaume A. M., Fougerouse D., Laurent A. T., Gardés E., Reddy S. M. and Saxey D. W. (2019) Nanoscale resetting of the Th/Pb system in an isotopically-closed monazite grain: A combined atom probe and transmission electron microscopy study. *Geosci. Front.* **10**, 65–76. Available at: https://doi.org/10.1016/j.gsf.2018.09.004.

Sharp T. G. and de Carli P. S. (2006) Shock effects in meteorites. *Meteorites Early Sol. Syst. II* **943**, 653–677. Available at: http://www.lpi.usra.edu/books/MESSII/9040.pdf.

Sharp Z., Williams J., Shearer C., Agee C. and McKeegan K. (2016) The chlorine isotope composition of Martian meteorites 2. Implications for the early solar system and the formation of Mars. *Meteorit. Planet. Sci.* **51**, 2111–2126. Available at: http://doi.wiley.com/10.1111/maps.12591.

Shearer C. K., Burger P. V., Papike J. J., McCubbin F. M. and Bell A. S. (2015) Crystal chemistry of merrillite from Martian meteorites: Mineralogical recorders of magmatic processes and planetary differentiation. *Meteorit. Planet. Sci.* **50**, 649–673.

Shearer C. K., Messenger S., Sharp Z. D., Burger P. V and Nguyen A. N. (2018) Distinct chlorine isotopic reservoirs on Mars . Implications for character , extent and relative timing of crustal interactions with mantle-derived magmas , evolution of the martian atmosphere , and the building blocks of an early Mars. *Geochim. Cosmochim. Acta* **234**, 24–36. Available at: https://doi.org/10.1016/j.gca.2018.04.034.

Słaby E., Förster H.-J., Wirth R., Giera A., Birski Ł. and Moszumańska I. (2017) Validity of the Apatite/Merrillite Relationship in Evaluating the Water Content in the Martian Mantle: Implications from Shergottite Northwest Africa (NWA) 2975. *Geosciences* **7**, 99. Available at: http://www.mdpi.com/2076-3263/7/4/99.

Slaby E., Koch-Müller M., Förster H. J., Wirth R., Rhede D., Schreiber A. and Schade U. (2016) Determination of volatile concentrations in fluorapatite of Martian shergottite NWA 2975 by combining synchrotron FTIR, Raman spectroscopy, EMPA, and TEM, and inferences on the volatile budget of the apatite host-magma. *Meteorit. Planet. Sci.* **51**, 390–406.

Snape J. F., Nemchin A. A., Grange M. L., Bellucci J. J., Thiessen F. and Whitehouse M. J. (2016) Phosphate ages in Apollo 14 breccias: Resolving multiple impact events with high precision U-Pb SIMS analyses. *Geochim. Cosmochim. Acta* **174**, 13–29. Available at: http://dx.doi.org/10.1016/j.gca.2015.11.005.

Stöffler D., Hamann C. and Metzler K. (2018) Shock metamorphism of planetary silicate rocks and sediments: Proposal for an updated classification system. *Meteorit. Planet. Sci.* **53**, 5–49.

Thompson K., Lawrence D., Larson D. J., Olson J. D., Kelly T. F. and Gorman B. (2007) In situ site-specific specimen preparation for atom probe tomography. *Ultramicroscopy*.

Thompson R. M., Xie X., Zhai S., Downs R. T. and Yang H. (2013) A comparison of the Ca3(PO4)2 and CaSiO3 systems, with a new structure refinement of tuite synthesized at 15 GPa and 1300 °C. *Am. Mineral.* **98**, 1585–1592.

Valley J. W., Cavosie A. J., Ushikubo T., Reinhard D. A., Lawrence D. F., Larson D. J., Clifton P. H., Kelly T. F., Wilde S. A., Moser D. E. and Spicuzza M. J. (2014) Hadean age for a post-magma-ocean zircon confirmed by atom-probe tomography. *Nat. Geosci.* **7**, 219–223. Available at: http://dx.doi.org/10.1038/ngeo2075%5Cnhttp://www.nature.com/ngeo/journal/v7/n3/abs/ngeo2075.html#supplementary-information%5Cnhttp://www.nature.com/doifinder/10.1038/ngeo2075.

Wang S. Z., Zhang A. C., Pang R. L., Chen J. N., Gu L. X. and Wang R. C. (2017) Petrogenesis and shock metamorphism of the enriched lherzolitic shergottite Northwest Africa 7755. *Meteorit. Planet. Sci.* **52**, 2437–2457.

Weis F. A., Bellucci J. J., Skogby H., Stalder R., Nemchin A. A. and Whitehouse M. J. (2017) Water content in the Martian mantle: A Nakhla perspective. *Geochim. Cosmochim. Acta* **212**, 84–98. Available at: http://dx.doi.org/10.1016/j.gca.2017.05.041.

White Lee F., Darling J. R., Moser D. E., Reinhard D. A., Dunlop J., Larson D. J., Lawrence D. and Martin I. (2017) Complex Nanostructures in Shocked, Annealed, and Metamorphosed Baddeleyite Defined by Atom Probe Tomography. In *Microstructural Geochronology: Planetary Records Down to Atom Scale* Geophysical Monograph Series. American Geophysical Union, United States. pp. 351–367. Available at: http://doi.wiley.com/10.1002/9781119227250.ch17.

White L. F., Darling J. R., Moser D. E., Reinhard D. A., Prosa T. J., Bullen D., Olson D., Larson D. J., Lawrence D. and Martin I. (2017) Atomic-scale age resolution of planetary events. *Nat. Commun.* **8**, 15597. Available at: http://www.nature.com/articles/ncomms15597.

White L. F., Moser D. E., Tait K., Langelier B., Barker I. R. and Darling J. (2018) Crystallization and impact history of a meteoritic sample of early lunar crust (NWA 3163) refined by atom probe geochronology. *Geosci. Front.*

Williams J. T., Shearer C. K., Sharp Z. D., Burger P. V., McCubbin F. M., Santos A. R., Agee C. B. and McKeegan K. D. (2016) The chlorine isotopic composition of Martian meteorites 1: Chlorine isotope composition of Martian mantle and crustal reservoirs and their interactions. *Meteorit. Planet. Sci.* **51**, 2092–2110. Available at: http://doi.wiley.com/10.1111/maps.12647.

Xie X., Minitti M. E., Chen M., Mao H. o-kwan., Wang D., Shu J. and Fei Y. (2002) Natural high-pressure polymorph of merrillite in the shock veins of the Suizhou meteorite. *Geochim. Cosmochim. Acta* **66**, 2439–2444. Available at: https://www.sciencedirect.com/science/article/pii/S0016703702008335 [Accessed June 22, 2018].

Xie X., Zhai S., Chen M. and Yang H. (2013) Tuite, γ-Ca3(PO4)2, formed by chlorapatite decomposition in a shock vein of the Suizhou L6 chondrite. *Meteorit. Planet. Sci.* **48**, 1515–1523.

Xie X., Yang H., Gu X. and Downs R. T. (2015) Chemical composition and crystal structure of merrillite from the Suizhou meteorite. *Am. Mineral.* **100**, 2753. Available at: http://dx.doi.org/10.2138/am-2015-5488.

Declaration of interests

☒ The authors declare that they have no known competing financial interests or personal relationships that could have appeared to influence the work reported in this paper.

☐The authors declare the following financial interests/personal relationships which may be considered as potential competing interests: